

# Cross Calibration of Imaging Air Cherenkov Telescopes with Fermi

Manuel Meyer, Hannes-Sebastian Zechlin, Dieter Horns  
*Institut für Experimentalphysik, University of Hamburg*  
*Luruper Chaussee 149 D-22767, Hamburg, Germany*  
 (Dated: March 2, 2022)

An updated model for the synchrotron and inverse Compton emission from a population of high energy electrons of the Crab nebula is used to reproduce the measured spectral energy distribution from radio to high energy  $\gamma$ -rays. By comparing the predicted inverse Compton component with recent Fermi measurements of the nebula's emission, it is possible to determine the average magnetic field in the nebula and to derive the underlying electron energy distribution. The model calculation can then be used to cross calibrate the Fermi observations with ground based air shower measurements. The resulting energy calibration factors are derived and can be used for combining broad energy measurements taken with Fermi in conjunction with ground based measurements.

## I. INTRODUCTION

The Crab Nebula is probably the best studied object in astrophysics (for a recent review see e.g. Hester [16]). It is the remnant of a core-collapse supernova which occurred in 1054 AD at a distance of  $d \approx 2$  kpc [27]. Near its geometric center resides a pulsar which continuously injects a wind of ultra-relativistic particles into the nebula. The wind terminates at a shock front where electrons are pitch angle isotropized, forming a broad power-law in energy.

Observations of the synchrotron and inverse Compton nebula have been carried out in every accessible wavelength resulting in a remarkably well known spectral energy distribution (SED). The large area telescope (LAT) onboard the Fermi satellite [26] has recently measured the flux of the  $\gamma$ -rays of the Crab between 100 MeV and 300 GeV with unprecedented accuracy.

These observations can be used for a cross calibration between the Fermi/LAT and ground based air shower experiments. This leads to the elimination of the systematic uncertainties on the absolute energy scale of typically 15 % for imaging air Cherenkov telescopes (IACTs).

For the cross calibration we use our approach presented in Meyer *et al.* [24]: based on the work of Hillas *et al.* [18], we extract the distribution of electrons from the synchrotron spectrum under the assumption of a constant magnetic field strength throughout the nebula. Using this electron distribution in conjunction with the seed photon fields as extracted from observations, we obtain a detailed prediction for the inverse Compton emission.

The average magnetic field inside the nebula is determined by fixing the model to the Fermi/LAT observations. The model can directly be used as the basis for the cross calibration. For this purpose energy scaling factors are derived to correct the measurements of the ground based instruments to the model.

The article is organized as follows. In section II the model for the SED is quickly reviewed, where the details and the discussion of the underlying electron spectrum are spared out and we refer the reader to Meyer *et al.* [24]. The results of the cross calibration are presented in section III together with an application to extract limits on the dif-

fuse  $\gamma$ -ray background at TeV energies. Section IV summarizes the article and gives a short outlook on possible future work.

## II. MODEL OF THE SPECTRAL ENERGY DISTRIBUTION OF THE CRAB NEBULA

A population of relativistic electrons is assumed to be distributed in a spherical volume following a Gaussian density distribution with its maximum at the nebula's center. The width of the Gaussian is parameterized in order to reproduce the shrinking size of the nebula with increasing frequency. The volume of the nebula is assumed to be filled with an entangled magnetic field of constant field strength. Within the volume occupied by the electrons, various seed photons are upscattered. The effective density of seed photons  $n_{\text{seed}}$  is simply found by convolving the electron density with the photon density [see 18, for further details]. The total emission from the nebula is then found by integration:

$$L_\nu = \int d\gamma n(\gamma) (\mathcal{L}_\nu^{\text{Sy}} + \mathcal{L}_\nu^{\text{IC}}), \quad (1)$$

with  $\mathcal{L}_\nu$  the single particle emission functions for synchrotron (Sy) and inverse Compton processes (IC) [see e.g. 9]:

$$\mathcal{L}_\nu^{\text{Sy}} = \frac{\sqrt{2}e^3 B}{mc^2} \frac{\nu}{\nu_c} \int_{\nu/\nu_c}^{\infty} K_{5/3}(x) dx, \quad (2)$$

$$\mathcal{L}_\nu^{\text{IC}} = \frac{3}{4} \frac{\sigma_{\text{T}}}{\gamma^2} h\nu \int_{h\nu/(4\gamma^2)}^{h\nu} d\epsilon \frac{n_{\text{seed}}(\epsilon)}{\epsilon} f_{\text{IC}}(\epsilon, \nu, \gamma), \quad (3)$$

where we have averaged the pitch angle to give  $\sqrt{2/3}$  and  $\sigma_{\text{T}}$  denotes the Thomson cross-section. The critical frequency  $\nu_c$  is defined as

$$\nu_c = \frac{3e}{4\pi mc} B \gamma^2, \quad (4)$$

and  $K_{5/3}(x)$  stands for the modified Bessel function of fractional order 5/3. Introducing the kinematic variable  $q$ ,

$$q = \frac{h\nu}{4\epsilon\gamma^2[1 - h\nu/(\gamma mc^2)]}, \quad (5)$$

the IC distribution function  $f_{IC}$  can be written as

$$f_{IC}(\epsilon, \nu, \gamma) = \frac{1}{2q \ln q + (1 + 2q)(1 - q)} + \frac{1}{2} \frac{[4\epsilon\gamma q/(mc^2)]^2}{1 + 4\epsilon\gamma q^2/(mc^2)} (1 - q). \quad (6)$$

For the inverse Compton channel photons from several seed photon fields are taken into account: (1) synchrotron radiation, (2) emission from thermal dust, (3) the cosmic microwave background (CMB), and (4) optical line emission from the nebula's filaments. The seed photon density  $n_{seed}$  in Eqn. 3 is the sum of all these components. Like the electron population, the spatial photon densities are approximated by Gaussian distributions whereas the photon density of the CMB is taken to be constant throughout the nebula. The spatial variance of these distributions is also energy dependent. The resulting broadband energy distribution is shown in Fig. 1. The electron spectrum is varied until the resulting synchrotron spectrum reproduces the observational data.

The compilation of data used here is summarized in Aharonian *et al.* [2] and references therein. Additionally, new data are added which are listed in Table I. The solid black curve in Fig. 1 is the sum of all contributions including synchrotron and IC emission as well as thermal emission from dust in the nebula and optical line emission from the filaments. For the thermal dust emission a graybody spectrum is used and a temperature of  $T = 93$  K was derived by fitting the combined spectrum (thermal and non-thermal emission) to the data (solid gray line in Fig. 1). The flux of the line emissions (orange solid line) is taken from Davidson [11], Davidson & Fesen [12] and Hester *et al.* [17]. The optical line emission of the filaments in the nebula is estimated in the following way: The high resolution spectral observations of individual filaments have been corrected for extinction [17] and scaled to match the global emission from the filaments [see e.g. the discussion in 12].

The FIR observations from Spitzer, ISO, and Scuba (orange and magenta circles in Fig. 1 respectively) deviate from the power-law extrapolation of the radio spectra. In the framework of two distinct electron populations, the shape of the continuum is naturally explained by the transition of the two synchrotron emission components.

The dashed blue curve indicates the total synchrotron and IC emission which results from the contributions from wind electrons whereas the dashed red line shows the contribution of the radio electrons. The dashed cyan lines show the total synchrotron and IC flux from both populations, respectively.

The electron spectrum was adapted such that the resulting synchrotron emission reproduces the power law measured with XMM-Newton. Both, the XMM-Newton and INTEGRAL (with the instruments SPI and IBIS/ISGRI) observatories are calibrated on the basis of detailed simulation and laboratory measurements. This approach differs from widely used corrections of the response function in

| Energy Band     | Instrument  | Reference                    |
|-----------------|-------------|------------------------------|
| Sub millimeter  | ISO & SCUBA | Green <i>et al.</i> [13]     |
| to far infrared | SPITZER     | Temim <i>et al.</i> [25]     |
| X-Ray to        | XMM-Newton  | Kirsch <i>et al.</i> [23]    |
| $\gamma$ -rays  | SPI         | Jourdain & Roques [19]       |
|                 | IBIS/ISGRI  | Jourdain <i>et al.</i> [20]  |
|                 | Fermi / LAT | The Fermi collaboration [26] |
| VHE             | H.E.S.S.    | Aharonian <i>et al.</i> [3]  |
|                 | MAGIC       | Albert <i>et al.</i> [5]     |

TABLE I: References for the observations used for the SED. All other data are taken from Aharonian *et al.* [2] and references therein.

order to re-produce a specific spectral shape and flux of the Crab nebula. The corrected measurements are therefore model-dependent and have not been included here. Furthermore, XMM-Newton is able to spatially resolve the Crab, whereas the measurement by SPI and IBIS/ISGRI may include contributions from the pulsar, possibly leading to higher fluxes in comparison to the XMM-Newton observations. Note, that the difference in flux normalization between XMM-Newton and SPI are beyond the systematic errors quoted. The model calculations shown here are fixed to the XMM-Newton spectra which then naturally underpredict the SPI measurements. The shape of the spectrum measured by SPI has been taken into account as both the power-law below 100 keV as well as above smoothly connect to the spectra measured at the low energy end by XMM-Newton and with Comptel at higher energies.

The predicted IC emission and the Fermi observations are used to determine the average magnetic field. This is shown in Fig. 2. The IC fluxes due to the different photon fields and electron populations add up to give the total black solid line. A standard  $\chi^2$ -minimization is used to determine the best value for the average  $B$ -field. Since a varying magnetic field also changes the synchrotron flux, the underlying electron spectrum is varied accordingly to compensate for the change, i.e. the synchrotron flux remains constant. Taking the systematic energy uncertainty on the global energy scale of the Fermi data into account,  $\Delta E/E = {}^{+5\%}_{-10\%}$  (sys.) [see e.g. 1], the average  $B$ -field is found to be

$$B = (124 \pm 6 \text{ (stat.) } {}^{+15}_{-6} \text{ (sys.)}) \mu\text{G}. \quad (7)$$

The discussion of this result in the light of MHD calculations [21] can be found in Meyer *et al.* [24]. It is worthwhile noting that the magnetic field derived here is less than half the value of the commonly used  $300 \mu\text{G}$ .

### A. The electron spectrum of the nebula

The underlying electron spectrum  $dN_{el}/d\gamma$  is the crucial quantity that determines the shape of the SED [see 24, for a

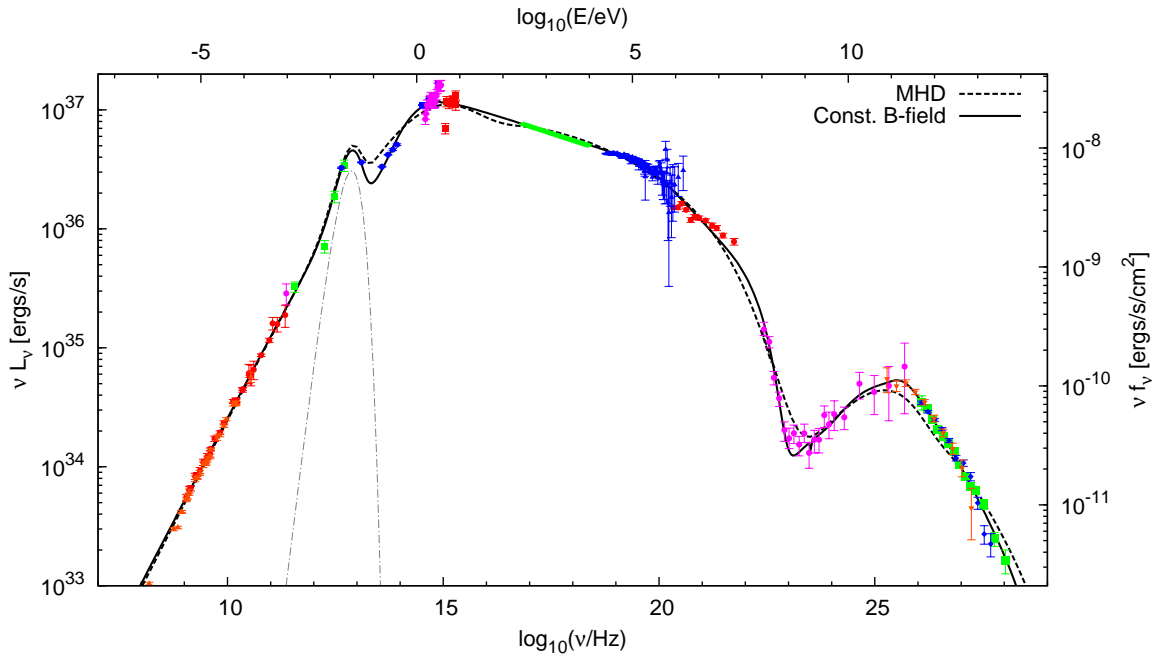


FIG. 1: Broadband SED of the Crab nebula. See section II for details. The two black curves correspond to the models described in Meyer *et al.* [24]

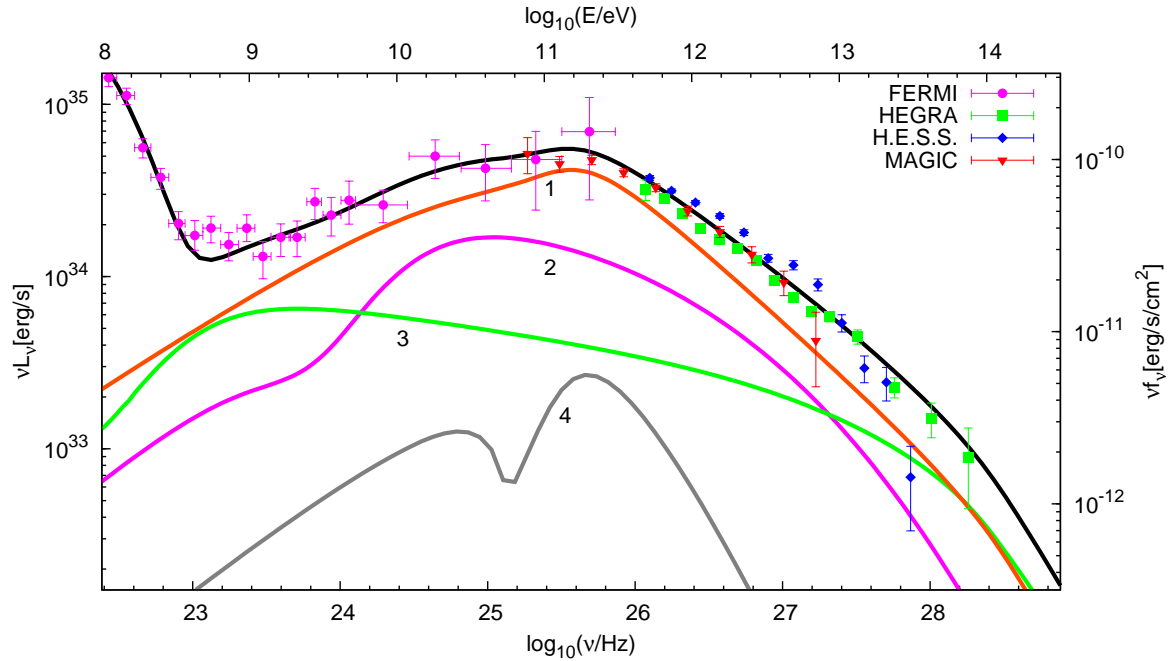


FIG. 2: The total IC flux due to different seed photon fields and the Fermi data points are shown. For the numbering see the text.

detailed discussion]. It consists of the two afore mentioned electron populations where the radio electron spectrum is given by

$$\frac{dN_{el}^r}{d\gamma} = \begin{cases} N_0^r \gamma^{-S_r} & \text{for } \gamma_1^r \leq \gamma \leq \gamma_2^r, \\ 0 & \text{otherwise,} \end{cases} \quad (8)$$

The radio electrons were probably injected in the phase of rapid spin-down during the initial stages of the pulsar-wind evolution [6]. The values for  $\gamma_0^r$ ,  $\gamma_1^r$ , and  $\gamma_2^r$  are summarized in Table II. Above  $\gamma_2^r$  and below  $\gamma_1^r$  a sharp cut-off for the spectrum is chosen, i.e.  $dN_{el}/d\gamma = 0$  for  $\gamma < \gamma_1^r$  and  $\gamma > \gamma_2^r$ .

The wind electrons produce via synchrotron emission the bulk of the observed SED above sub-mm/FIR wave-

| Population | $N_0$    | $\ln \gamma_0$ | $\ln \gamma_1$ | $\ln \gamma_2$ | $S$     |
|------------|----------|----------------|----------------|----------------|---------|
| Radio      | 120.0(1) | –              | 3.1            | 12.1(7)        | 1.60(1) |
| Wind       | 78.6(3)  | 19.5(1)        | 12.96(3)       | 22.51(3)       | 3.23(1) |

TABLE II: Cut-off and normalization energies together with the spectral indices  $S$  of the electron spectrum. See text and Eqn. 9 for further details.

lengths. The wind electrons are constantly injected downstream of the wind shock (hence the name). The radiatively cooled spectrum of the wind electron has a spectral index of  $S_w = 3.23 = 2.23 + 1$  which can naturally be explained by ultra-relativistic 1<sup>st</sup> order Fermi acceleration with synchrotron cooling [see e.g. 22].

An additional feature present in the hard X-ray spectrum which follows a broken power-law with a break at  $\sim 70$  keV requires a break with  $\Delta S = 0.43$  in the electron-spectrum. We tentatively relate this break to the injection mechanism, given that it can hardly be related to energy dependent escape (the X-ray emitting electrons suffer cooling well before escaping the nebula). The value of  $\Delta S$  could hint at an energy dependent effect similar to diffusion in a Kolmogorov-type turbulence power spectrum. For high and low energies the wind electron spectrum cuts off super-exponentially,

$$\frac{dN_{\text{el}}^w}{d\gamma} = N_0^w \left\{ \begin{array}{ll} \left(\frac{\gamma}{\gamma_0^w}\right)^{-S_w}, & \text{for } \gamma < \gamma_0^w, \\ \left(\frac{\gamma}{\gamma_0^w}\right)^{-(S_w+\Delta S)}, & \text{for } \gamma_0^w \leq \gamma \leq \gamma_2^w, \\ 0, & \text{for } \gamma > \gamma_2^w, \end{array} \right\} \times \exp\left(-\left[\frac{\gamma_1^w}{\gamma}\right]^{2.8(4)}\right). \quad (9)$$

where the values for  $\gamma_0^w$ ,  $\gamma_1^w$  and  $\gamma_2^w$  are listed in Table II. The total energy of the radio and wind electrons, respectively is found to be

$$E_r = mc^2 \int_1^\infty \gamma \frac{dN_{\text{el}}^r}{d\gamma} d\gamma = 3.10 \times 10^{48} \text{ ergs}, \quad (10)$$

$$E_w = mc^2 \int_1^\infty \gamma \frac{dN_{\text{el}}^w}{d\gamma} d\gamma = 2.28 \times 10^{48} \text{ ergs}, \quad (11)$$

indicating that the total energy is much smaller than the integrated energy released through the spin-down of the pulsar. The fact that both relic electrons and wind electrons share roughly equal energy is probably coincidental.

### III. CROSS CALIBRATION OF IACTS & FERMI

The updated model of the SED of the Crab Nebula provides an opportunity for the cross calibration between ground based air shower experiments and the Fermi large area telescope. The method is demonstrated here with the imaging air Cherenkov telescopes (IACTs) HEGRA,

H.E.S.S. and MAGIC but is applicable to any other ground based air shower experiment.

The energy calibration of IACTs is done indirectly with the help of detailed simulations of air showers and the detector response. However, the remaining systematic uncertainty on the absolute energy scale of typically 15 % leads to substantial differences in the observed flux and position of cut-offs in the energy spectra between different IACTs and also between Fermi/LAT and IACTs.

Since the observed energy spectra are usually quite broad in energy, the position of features in the spectra are not useful (and may be time-dependent for some objects) for cross calibration. On the other hand, cross calibration between Fermi/LAT and IACTs provides indirectly a means of benefitting from the careful beam-line calibration of the Fermi/LAT [see e.g. 8]. For this reason, the average magnetic field used in the model was fixed to Fermi observations.

The cross calibration is now accomplished in the following way: for each IACT an energy scaling factor  $s_{\text{IACT}}$  is introduced such that

$$E' = E \cdot s_{\text{IACT}}. \quad (12)$$

The scaling factor  $s_{\text{IACT}}$  is determined via a  $\chi^2$ -minimization in which the energy scale is changed according to the formula above until the data points reproduce the model best. The scaling factors for the different instruments are listed in Table III together with the statistical errors and the reduced  $\chi^2$  values of the fit. The statistical uncertainties were obtained by summing the errors of the  $\chi^2$ -fit and the statistical errors of the model in quadrature. The latter are mainly due to the uncertainties on the  $B$ -field of Eqn. 7. To illustrate the result, Figure 3(a) and 3(b) compare the unscaled data points of the Crab nebula with the scaled ones. It is evident that the data points fit the model better after scaling. All scaling factors lie within the afore mentioned 15 % energy uncertainty of the IACTs.

The application of the cross calibration eliminates the systematic uncertainty of the energy scale of the IACTs and adjusts the energy scale to the one of the Fermi/LAT. Since the model relies on the Fermi/LAT measurements, the Fermi/LAT's absolute energy uncertainty remains. This implies an improvement for the systematic uncertainty on the energy scale of IACT measurements from  $\pm 15\%$  to  ${}^{+5\%}_{-10\%}$ . However, the model itself also contributes to the systematic uncertainties. The main uncertainty stems from the fact that a constant magnetic field is assumed which is very likely not the case. It should be also noted, that the cross calibration factors hinge mainly on the high statistics measurement of the IACTs at low TeV-

energies which are produced by electrons that co-exist in the same volume in the nebula as the electrons emitting at lower energies (i.e. in the Fermi/LAT energy range).

As a first application of the cross calibration, we derive upper limits on the diffuse  $\gamma$ -ray background.

Both Fermi [1], and H.E.S.S. [4, 15] have measured the cosmic ray  $e^- + e^+$  spectrum. Unlike Fermi, the telescopes from H.E.S.S. cannot accurately distinguish between showers induced by electrons (or positrons) or photons, such that up to  $\approx 50\%$  of the observed electromagnetic air showers could be induced by photons. Hence, H.E.S.S. actually measures electrons and diffuse background photons. Taking the difference of the two measurements we can derive an upper limit on the flux of the  $\gamma$ -ray background. The scaling factors derived above are now used to convert the IACT data to the same energy scale of Fermi, which reduces substantially the systematic uncertainty on the observed flux given that the electron spectrum follows a soft power-law with  $E^{-3}$ .

The upper limits were derived by subtracting the two fluxes from the overlapping region of the measurements. This corresponds to the first six H.E.S.S. points of the low energy analysis in Figure 4. The remaining systematic energy uncertainties, denoted by the green and yellow bowties, were taken into account for the derivation of the upper limits: the flux points of the H.E.S.S. measurements were shifted to their maximum value allowed by the systematic uncertainties while the Fermi points were shifted to the minimum value. Hence, the result represents a conservative approximation of the upper limits.

An important result of the cross calibration is that the peak in the spectrum observed by ATIC [10] appears more unlikely after applying the scaling factors.

#### IV. SUMMARY AND OUTLOOK

An updated model for the SED of the Crab nebula has been introduced. It incorporates a new electron spectrum

that consists of two electron populations that have been studied extensively in the past [see e.g. 6, 7].

The average  $B$ -field was derived by fixing the IC flux to Fermi/LAT measurements.

The model makes it possible to derive energy scaling factors that eliminate the systematic energy uncertainties of ground based air shower experiments. An application of the cross calibration to the diffuse  $\gamma$ -background has been presented and upper limits have been derived. Moreover, the excess measured by the ATIC collaboration seems unlikely with the scaled H.E.S.S. observations.

Nevertheless, an improved model for the emission of the Crab is conceivable. Such a model could comprise a spatially varying  $B$ -field and hence the fact that electrons emitting different energies are exposed to different field strengths.

To conclude, a way to establish the Crab as a *true* standard candle in  $\gamma$ -ray astronomy has been presented and versatile applications to other observations of bright steady or pulsed sources (e.g. the Crab Pulsar, the Galactic Center other Pulsar Wind Nebulae, etc.) are imaginable. Moreover, an application of the cross calibration will help to improve dark matter searches and constraints on the extra galactic background light.

#### Acknowledgments

The participation of the Fermi Symposium was made possible with the support of the German federal ministry for education and research (Bundesministerium für Bildung und Forschung).

It was also supported by the collaborated research center (SFB) 676 “Particle, Strings and the early Universe” at the University of Hamburg.

- 
- [1] ABDO, A. A., ACKERMANN, M., & THE FERMI COLLABORATION. 2009. Measurement of the Cosmic Ray  $e^+ + e^-$  Spectrum from 20 GeV to 1 TeV with the Fermi Large Area Telescope. *Physical Review Letters*, **102**(18), 181101–+.
- [2] AHARONIAN, F., AKHPERJANIAN, & THE HEGRA COLLABORATION. 2004. The Crab Nebula and Pulsar between 500 GeV and 80 TeV: Observations with the HEGRA Stereoscopic Air Cerenkov Telescopes. *Astrophys. J.*, **614**(Oct.), 897–913.
- [3] AHARONIAN, F., AKHPERJANIAN, & THE HESS COLLABORATION. 2006. Observations of the Crab nebula with HESS. *Astron. Astrophys.*, **457**(Oct.), 899–915.
- [4] AHARONIAN, F., AKHPERJANIAN, A. G., BARRES DE ALMEIDA, U., & BAZER-BACHI, A. R. 2008. Energy Spectrum of Cosmic-Ray Electrons at TeV Energies. *Physical Review Letters*, **101**(26), 261104–+.
- [5] ALBERT, J., ALIU, & THE MAGIC COLLABORATION. 2008. VHE  $\gamma$ -Ray Observation of the Crab Nebula and its Pulsar with the MAGIC Telescope. *Astrophys. J.*, **674**(Feb.), 1037–1055.
- [6] ATOYAN, A. M. 1999. Radio spectrum of the Crab nebula as an evidence for fast initial spin of its pulsar. *Astron. Astrophys.*, **346**(June), L49–L52.
- [7] ATOYAN, A. M., & AHARONIAN, F. A. 1996. On the mechanisms of gamma radiation in the Crab Nebula. *Mon. Not. R. Astron. Soc.*, **278**(Jan.), 525–541.
- [8] ATWOOD, W. B., ABDO, A. A., & THE FERMI COLLABORATION. 2009. The Large Area Telescope on the Fermi Gamma-Ray Space Telescope Mission. *Astrophys. J.*, **697**(June), 1071–1102.
- [9] BLUMENTHAL, G. R., & GOULD, R. J. 1970. Bremsstrahlung, Synchrotron Radiation, and Compton Scattering of High-Energy Electrons Traversing Dilute Gases. *Reviews of Mod-*

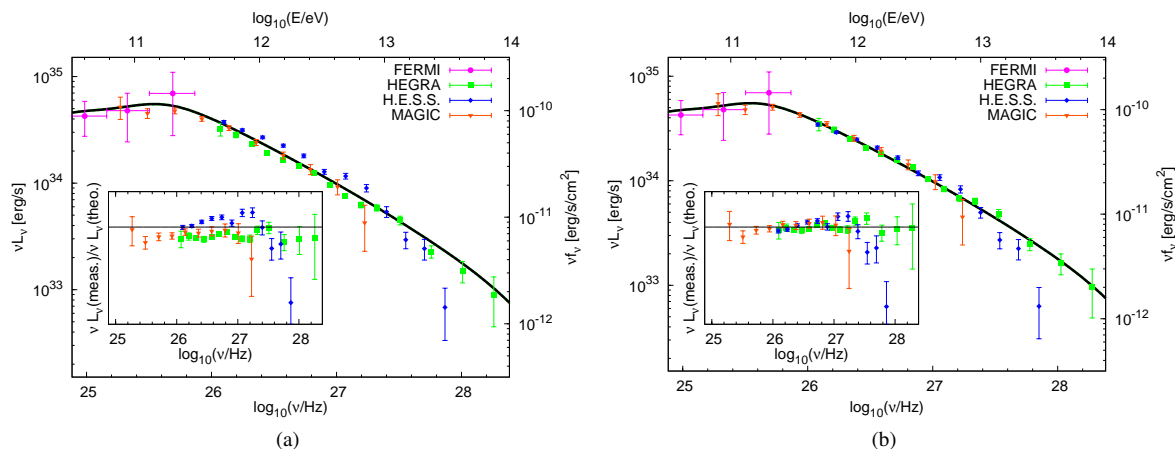


FIG. 3: (a) The IC model (solid black line) together with measurements from IACTs and Fermi. No Energy scaling is applied. (b) The same situation as in 3(a) but with the scaling factors of Eqn. 12 and Table III applied. The open squares denote H.E.S.S. points that were not included in the fit due to the high systematic uncertainty of the highest energy measurements.

TABLE III: Energy scaling factors of the IACTs for the cross calibration.

| Instrument | Scaling factor $s_{\text{IACT}}$ | Stat. error $\Delta s$ | $\chi^2_{\text{before}}/\text{d.o.f.}$ | $\chi^2_{\text{after}}/\text{d.o.f.}$ |
|------------|----------------------------------|------------------------|--|---------------------------------------|
| Fermi/LAT  | 1                                | +0.05 - 0.03           | —                                      | 0.49                                  |
| HEGRA      | 1.042                            | $\pm 0.005$            | 7.652                                  | 1.046                                 |
| H.E.S.S.   | 0.961                            | $\pm 0.004$            | 11.84                                  | 6.476                                 |
| MAGIC      | 1.03                             | $\pm 0.01$             | 1.671                                  | 0.656                                 |

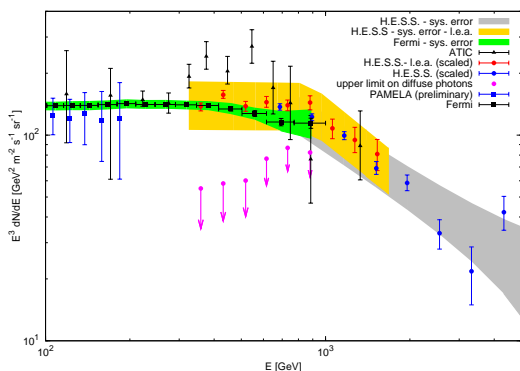


FIG. 4:  $e^- + e^+$  Spectrum reported by H.E.S.S. and Fermi. The cross calibration is applied, hence the uncertainty on the global energy scale is eliminated.

*ern Physics*, **42**, 237–271.

- [10] CHANG, J., ADAMS, J. H., AHN, H. S., BASHINDZHAGYAN, G. L., CHRISTL, M., GANEL, O., GUZIK, T. G., ISBERT, J., KIM, K. C., KUZNETSOV, E. N., PANASYUK, M. I., PANOV, A. D., SCHMIDT, W. K. H., SEO, E. S., SOKOLSKAYA, N. V., WATTS, J. W., WEFEL, J. P., WU, J., & ZATSEPIN, V. I. 2008. An excess of cosmic ray electrons at energies of 300-800GeV. *Nature (London)*, **456**(Nov.), 362–365.
- [11] DAVIDSON, K. 1987. Spectrophotometry of the Crab Nebula as a whole. *Astron. J.*, **94**(Oct.), 964–971.
- [12] DAVIDSON, K., & FESEN, R. A. 1985. Recent developments concerning the Crab Nebula. *Ann. Rev. Astron. Astrophys.*,

**23**, 119–146.

- [13] GREEN, D. A., TUFFS, R. J., & POPESCU, C. C. 2004. Far-infrared and submillimetre observations of the Crab nebula. *Mon. Not. R. Astron. Soc.*, **355**(Dec.), 1315–1326.
- [14] HARDING, A. K., & DE JAGER, O. C. 1992. Constraints on electron acceleration in the Crab nebula. *Pages 471–476 of: G. P. ZANK & T. K. GAISSER (ed), Particle Acceleration in Cosmic Plasmas*. American Institute of Physics Conference Series, vol. 264.
- [15] H.E.S.S. COLLABORATION: F. AHARONIAN. 2009. Probing the ATIC peak in the cosmic-ray electron spectrum with H.E.S.S. *ArXiv e-prints*, May.
- [16] HESTER, J. J. 2008. The Crab Nebula: An Astrophysical Chimera. *Ann. Rev. Astron. Astrophys.*, **46**(Sept.), 127–155.
- [17] HESTER, J. J., GRAHAM, J. R., BEICHMAN, C. A., & GAUTIER, III, T. N. 1990. Infrared and optical imagery of the Crab Nebula. *Astrophys. J.*, **357**(July), 539–547.
- [18] HILLAS, A. M., AKERLOF, C. W., & OTHERS. 1998. The Spectrum of TeV Gamma Rays from the Crab Nebula. *Astrophys. J.*, **503**(Aug.), 744–.
- [19] JOURDAIN, E., & ROQUES, J. P. 2009. The High-Energy Emission of the Crab Nebula from 20 keV TO 6 MeV with Integral SPI. *Astrophys. J.*, **704**(Oct.), 17–24.
- [20] JOURDAIN, E., GÖTZ, D., WESTERGAARD, N. J., NATALUCCI, L., & ROQUES, J. P. 2008. INTEGRAL Cross-calibration Status: Crab observations between 3 keV and 1 MeV. *In: Proceedings of the 7th INTEGRAL Workshop. 8 - 11 September 2008 Copenhagen, Denmark*. Online at <http://pos.sissa.it/cgi-bin/reader/conf.cgi?confid=67>, p.144.
- [21] KENNEL, C. F., & CORONITI, F. V. 1984. Confinement of the Crab pulsar’s wind by its supernova remnant. *Astrophys. J.*

- , **283**(Aug.), 694–709.
- [22] KIRK, J. G., & SCHNEIDER, P. 1986. On the acceleration of charged particles at relativistic shock-fronts. *MPA Rep.*, No. 239, 22 pp., **239**.
- [23] KIRSCH, M. G., BRIEL, U. G., & OTHERS. 2005 (Aug.). Crab: the standard x-ray candle with all (modern) x-ray satellites. Pages 22–33 of: SIEGMUND, O. H. W. (ed), *Society of Photo-Optical Instrumentation Engineers (SPIE) Conference Series*. Society of Photo-Optical Instrumentation Engineers (SPIE) Conference Series, vol. 5898.
- [24] MEYER, M., HORNS, D., & ZEHLIN, H. S. 2010. The Crab Nebula as the standard Candle in Very High Energy Astrophysics. *To be published in Astron. Astrophys.*.
- [25] TEMIM, T., GEHRZ, R. D., & OTHERS. 2006. Spitzer Space Telescope Infrared Imaging and Spectroscopy of the Crab Nebula. *Astron. J.*, **132**(Oct.), 1610–1623.
- [26] THE FERMI COLLABORATION. 2009. Fermi Large Area Telescope Observations of the Crab Pulsar and Nebula. *ArXiv e-prints: 0911.2412*, Nov.
- [27] TRIMBLE, V. 1968. Motions and Structure of the Filamentary Envelope of the Crab Nebula. *Astron. J.*, **73**(Sept.), 535–+.
- [28] VOLPI, D., DEL ZANNA, L., AMATO, E., & BUCCIANINI, N. 2008. Non-thermal emission from relativistic MHD simulations of pulsar wind nebulae: from synchrotron to inverse Compton. *Astron. Astrophys.*, **485**(July), 337–349.
- [29] ZHANG, L., CHEN, S. B., & FANG, J. 2008. Nonthermal Radiation from Pulsar Wind Nebulae. *Astrophys. J.*, **676**(Apr.), 1210–1217.